



Generating porosity spectrum of carbonate reservoirs using ultrasonic imaging log

Jie Zhang^{1,2} · Xin Nie^{1,2,3} · Suyun Xiao⁴ · Chong Zhang^{1,2} · Chaomo Zhang^{1,2} · Zhansong Zhang^{1,2}

Received: 21 December 2017 / Accepted: 24 March 2018 / Published online: 31 March 2018
© Institute of Geophysics, Polish Academy of Sciences & Polish Academy of Sciences 2018

Abstract

Imaging logging tools can provide us the borehole wall image. The micro-resistivity imaging logging has been used to obtain borehole porosity spectrum. However, the resistivity imaging logging cannot cover the whole borehole wall. In this paper, we propose a method to calculate the porosity spectrum using ultrasonic imaging logging data. Based on the amplitude attenuation equation, we analyze the factors affecting the propagation of wave in drilling fluid and formation and based on the bulk-volume rock model, Wyllie equation and Raymer equation, we establish various conversion models between the reflection coefficient β and porosity ϕ . Then we use the ultrasonic imaging logging and conventional wireline logging data to calculate the near-borehole formation porosity distribution spectrum. The porosity spectrum result obtained from ultrasonic imaging data is compared with the one from the micro-resistivity imaging data, and they turn out to be similar, but with discrepancy, which is caused by the borehole coverage and data input difference. We separate the porosity types by performing threshold value segmentation and generate porosity–depth distribution curves by counting with equal depth spacing on the porosity image. The practice result is good and reveals the efficiency of our method.

Keywords Carbonate reservoir · Porosity spectrum · Well logging analysis · Ultrasonic imaging logging

List of symbols

A	Amplitude, L , m
f	Frequency, $1/t$, Hz
L	Propagation distance, L , m
\bar{L}	Average distance from the transducer to the borehole wall at the same depth, L , m
m	The ratio of number of pixels, n/n , 1
n	Unit volume particle number, n , 1
r	Radius of spherical particles, L , m
v	Wave propagation speed, L/t , m/s
v_0	Ultrasonic transmission speed in the drilling mud, L/t , m/s
V_{sh}	Shale volume content, L^3/L^3 , %

Z	Wave impedance, m/L^2t , g/cm^3 m/s
α	Amplitude attenuation coefficient, L/L , 1
β	Reflection coefficient, L/L , 1
Δt	Near-borehole formation interval transit time, t , s
Δt_w	Water interval transit time, t , s
Δt_{ma}	Matrix interval transit time, t , s
Δt_{sh}	Shale interval transit time, t , s
λ	Wavelength of ultrasound, L , m
μ	Medium viscosity, mt/L^2 , Pa s
μ_0	Kinematic viscosity of fluid, mt/L^2 , Pa s
ρ	Density, m/L^3 , g/m^3
ρ_0	Density of fluid, m/L^3 , g/m^3
ρ_2	Near-bore formation density, m/L^3 , g/m^3
ρ_{ma}	Density of matrix, m/L^3 , g/m^3
ρ_s	Density of particles, m/L^3 , g/m^3
ρ_w	Density of water/fluid, m/L^3 , g/m^3
τ	Attenuation factor, L/L , 1
ϕ	Porosity, L^3/L^3 , %
ϕ_0	Foreground average porosity, L^3/L^3 , %
ϕ_1	Background average porosity, L^3/L^3 , %

✉ Xin Nie
xin.nie@yangtzeu.edu.cn

¹ Key Laboratory of Exploration Technologies for Oil and Gas Resources (Yangtze University), Wuhan 430100, Hubei, China

² School of Geophysics and Oil Resource, Yangtze University, Wuhan 430100, Hubei, China

³ Georgia Institute of Technology, Atlanta, GA 30332, USA

⁴ Jiangnan Oilfield Branch of Sinopec Group, Qianjiang 433124, Hubei, China

Introduction

There are two types of porosity in carbonate reservoirs including primary and secondary porosity, and the secondary porosity (includes vugs and fractures, etc.) whose structures and morphologies vary in different directions. Normally we use acoustic logging data to calculate the porosity. The usage of acoustic logging data is only limited to calculate the porosity through the wave velocity, not to reveal the pore structure property (Wang and Tao 2011; Wang et al. 2017). The conventional acoustic tools cannot provide the full azimuth information of the borehole. In practice, when the conditions of measurement and data acquired are limited, it is always a challenge to obtain the porosity distribution (Gu et al. 2017). Therefore, to accurately predict the production potential by conventional wireline logging was difficult. Accuracy has been greatly improved since micro-resistivity and ultrasonic borehole image logging was introduced to the industry. With the help of imaging logging, we can reveal the fracture density, orientation (e.g., dip and azimuth) and distribution of the fractures and caves visually in open hole. Based on the classic Archie saturation equation for the flushed zone, Newberry et al. (1996) proposed a method to convert micro-resistivity borehole images to porosity distribution of the formation. Using this method, we can obtain porosity spectrum which can be used in fine quantitative evaluation of the distribution of reservoir porosity. Predecessors have done much study on quantitatively evaluating the porosity distribution of carbonate reservoirs, and the application results were good (e.g., Hurley et al. 1998; Akbar et al. 2000; Tyagi and Bhaduri 2002, Xu et al. 2006; Ghafoori et al. 2009; Tetsushi et al. 2013). However, the micro-resistivity tool cannot cover the whole borehole wall, which causes white stripes between the pads. Therefore, information is lost in the process, especially in the section where high-angle fractures and vugs develop. The ultrasonic image can cover 100% borehole wall, therefore, it can provide more complete information. However, the advanced usage of ultrasonic imaging logging data has been studied by very few. In this paper, we analyze the factors affecting the propagation of wave in drilling mud and formation, and propose a new method which is based on the amplitude attenuation equation. Using this method, we can calculate the near-borehole formation porosity distribution with ultrasonic borehole images and conventional wireline logs.

Analysis of influence factors on the ultrasonic imaging logging

Ultrasonic imaging tool uses a rotating transducer to launch ultrasonic pulse traveling through borehole fluid, receives the echo of the borehole wall, and records the echo amplitude

and traveling time. Geological information, such as changes of lithology and physical properties, can be obtained using this tool. The measured echo amplitude is associated with the acoustic impedance and the shapes of the borehole wall. When the borehole diameter is “on gauge” (i.e. regular, without caves or key seats), the greater the acoustic impedance of the rock is, the larger the echo amplitude will be. Echo traveling time is associated with the geometric shape of borehole and the mud; as the mud is considered uniformly distributed in the borehole, it only reflects the status of borehole wall. The images reflect wave response from the surface of the borehole, thus can reveal the cracks and holes, similar to the micro-resistivity imaging.

The sound wave amplitude will decay exponentially with the changing of propagation distance in the medium. When passed through the medium interfaces, sound waves will result in refraction and reflection. Due to the difference of wave impedance, the reflection coefficient is different. According to the propagation distance and the differences of the two media, when the wave passes through the interface vertically, the reflection wave amplitude can be expressed as (Wang 2011):

$$A_1(f) = A_0(f) \times \beta \times e^{-\alpha(f,\mu) \times L}, \quad (1)$$

where $A_1(f)$ is the reflection wave amplitude traveling from the interface of medium 1 and 2 for time t ; $A_0(f)$ is the amplitude of the original wave launched by the acoustic transmitter in frequency f ; β is the reflection coefficient; $\alpha(f, \mu)$ is the amplitude attenuation coefficient, which is a function of sound wave frequency f and medium viscosity μ ; L is the propagation distance.

For an ultrasonic imaging logging tool, the acoustic transmitting frequency f is fixed; and at the same depth, borehole diameter is also a constant. Therefore, based on the analysis of Eq. (1), we identify two major factors that influence the ultrasonic echo amplitude: (1). attenuation coefficient α and (2) reflection coefficient β .

The influence of attenuation coefficient α

Ultrasonic attenuation process is complicated and difficult to analyze. One general equation of attenuation coefficient in fluid was presented by Urick (1948) and Urick and Ament (1949):

$$\alpha = \frac{2}{3} \pi r^3 n \left[\frac{1}{3} k^4 r^3 + k \left(\frac{\rho_s}{\rho_f} - 1 \right)^2 \frac{S}{S^2 + \left(\frac{\rho_s}{\rho_f} - \tau \right)} \right], \quad (2)$$

where $k = \frac{2\pi}{\lambda}$, $S = \frac{9\sigma}{4r} \left(1 + \frac{\sigma}{r} \right)$, $\tau = \frac{1}{2} + \frac{9\sigma}{4r}$ and $\sigma = \frac{2\mu_0}{\rho_0 \omega}$.

In Eq. (2), r is the radius of spherical particles, m; ρ_s is the density of particles, g/m³; ρ_0 is the density of fluid, g/m³; μ_0 is the kinematic viscosity of fluid, Pa s; λ is the wavelength of ultrasound, m; n is the unit volume particle

number; ω is the angular frequency, rad/s. According to Eq. (2), the influencing factors of attenuation coefficient α can be summed up into three classes: (a) micro-mud slurry: unit volume particle number n , radius of spherical particles r , density of particles ρ_s . (b) Macro-mud slurry: fluid density ρ_0 , fluid kinematic viscosity μ_0 . (c) Tool specification: tool transmitting frequency f , angular frequency ω , wavelength λ .

Therefore, it is obvious that the attenuation coefficient α just reflects the characteristics of the tool and drilling mud, but do not reflect the formation porosity.

The influence of reflection coefficient β

Z_1 and Z_2 are the wave impedance of drilling mud and formation, respectively; ρ and v are density and sound wave propagation speed. For the normal angle of incidence, their relationship with β can be shown as follows:

$$\beta = \frac{Z_2 - Z_1}{Z_2 + Z_1}. \quad (3a)$$

As Eq. (3a) shows, the main factors affecting reflection coefficient β are drilling mud and formation wave impedance Z_1 and Z_2 . And the formation wave impedance Z_2 can be expressed as follows:

$$Z_2 = \rho_2 v_2 = \frac{\rho_2}{\Delta t_2}, \quad (3b)$$

where ρ_2 is the near-borehole formation density; Δt_2 is the near-borehole interval transit time. Both ρ_2 and Δt_2 can reflect formation porosity changes, so the reflection coefficient β can be used as a tool to obtain the formation porosity.

Porosity conversion models

Reflection coefficient around the well bore mainly reflects the information near the interface where the pore has been flushed by drilling mud filtrate. The pore fluid near the borehole can be considered to be pure brine. Therefore, two models of pure matrix (matrix built up only by pure carbonate minerals such as calcite or dolomite) and argillaceous matrix (matrix built up with both carbonate minerals and clay minerals) can be established (Fig. 1).

Wyllie time average equation

Pure matrix model (Fig. 1a) satisfies the Wyllie time average equation (Wyllie equation, Wyllie et al. 1956, 1958), which can be written as:

$$\begin{cases} \rho_2 = \rho_w \phi + (1 - \phi)\rho_{ma} \\ \Delta t_2 = \Delta t_w \phi + (1 - \phi)\Delta t_{ma} \end{cases}. \quad (4a)$$

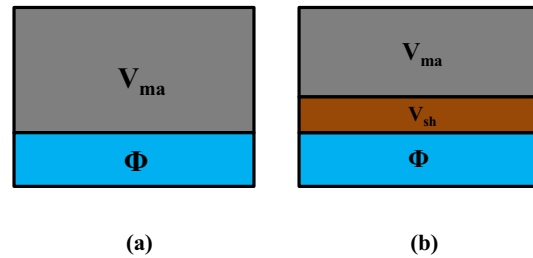


Fig. 1 Pure matrix model (a) and argillaceous matrix model (b)

Plug Eqs. (3b) and (4a) into Eq. (3a):

$$\begin{aligned} \beta &= \frac{Z_2 - Z_1}{Z_2 + Z_1} = \frac{\rho_2 v_2 - Z_1}{\rho_2 v_2 + Z_1} \\ &= \frac{\rho_{ma} - Z_1 \Delta t_{ma} + [(\rho_w - \rho_{ma}) - Z_1 (\Delta t_w - \Delta t_{ma})] \phi}{\rho_{ma} + Z_1 \Delta t_{ma} + [(\rho_w - \rho_{ma}) + Z_1 (\Delta t_w - \Delta t_{ma})] \phi}. \end{aligned} \quad (4b)$$

Let

$$\begin{aligned} a &= (\rho_w - \rho_{ma}) - Z_1 (\Delta t_w - \Delta t_{ma}); & b &= \rho_{ma} - Z_1 \Delta t_{ma}; \\ c &= (\rho_w - \rho_{ma}) + Z_1 (\Delta t_w - \Delta t_{ma}); & d &= \rho_{ma} + Z_1 \Delta t_{ma}; \end{aligned}$$

Then

$$\beta = \frac{Z_2 - Z_1}{Z_2 + Z_1} = \frac{\rho_2 v_2 - Z_1}{\rho_2 v_2 + Z_1} = \frac{a}{c} + \frac{b - \frac{a}{c}d}{c\phi + d} \quad (4c)$$

Let

$$A = \frac{a}{c} \quad \text{and} \quad B = b - \frac{a}{c}d$$

Then

$$\beta = \frac{Z_2 - Z_1}{Z_2 + Z_1} = \frac{\rho_2 v_2 - Z_1}{\rho_2 v_2 + Z_1} = A + \frac{B}{c\phi + d} \quad (4d)$$

Based on Eq. (4d), we can reveal the relationship between reflection coefficient and porosity in both pure calcite and dolomite matrix (Fig. 2). As the figure shows: (a) when the drilling mud wave impedance is constant, the greater the porosity is, the smaller the reflection coefficient is; (b) when the porosity is greater than 0.15 in limestone with pure calcite matrix and 0.25 in dolostone with pure dolomite matrix, the calculated reflection coefficients are larger than the experimental value (Chelini et al. 1998).

Therefore, when the drilling mud wave impedance is known, the porosity can be calculated with the reflection coefficient based on this model.

Raymer equation

As Fig. 2 shows, when porosity is larger than a certain value, the reflection coefficients converted by the above model do not conform to the actual situation. Consequently, we combine rock volume model and Raymer

conversion equation (Raymer equation, Raymer et al. 1980) to get the equations:

$$\begin{cases} \rho_2 = \rho_w \phi + (1 - \phi) \rho_{ma} \\ v_2 = v_w \phi + (1 - \phi) v_{ma} \\ \beta = \frac{Z_2 - Z_1}{Z_2 + Z_1} = \frac{\rho_2 v_2 - Z_1}{\rho_2 v_2 + Z_1} \end{cases} \quad (5)$$

Based on Eq. (5), the relationship between reflection coefficient and porosity can be calculated after a loop iteration (Fig. 3).

Argillaceous matrix model

Similar to the pure matrix model, argillaceous matrix model (Fig. 1b) satisfies the following equations:

$$\begin{cases} \rho_2 = \rho_w \phi + V_{sh} \rho_{sh} + (1 - \phi - V_{sh}) \rho_{ma} \\ \Delta t_2 = \Delta t_w \phi + V_{sh} \Delta t_{sh} + (1 - \phi - V_{sh}) \Delta t_{ma} \end{cases}, \quad (6a)$$

where V_{sh} is the shale content. Plug Eq. (6a) into Eq. (3a):

$$\beta = \frac{Z_2 - Z_1}{Z_2 + Z_1} = \frac{\rho_2 v_2 - Z_1}{\rho_2 v_2 + Z_1} = \frac{\rho_{ma} - Z_1 \Delta t_{ma} + (\rho_{sh} - \rho_{ma} - Z_1 \Delta t_{sh} + Z_1 \Delta t_{ma}) V_{sh} + [(\rho_w - \rho_{ma}) - Z_1 (\Delta t_w - \Delta t_{ma})] \phi}{\rho_{ma} + Z_1 \Delta t_{ma} + (\rho_{sh} - \rho_{ma} + Z_1 \Delta t_{sh} - Z_1 \Delta t_{ma}) V_{sh} + [(\rho_w - \rho_{ma}) + Z_1 (\Delta t_w - \Delta t_{ma})] \phi}. \quad (6b)$$

After simplification

$$\beta = \frac{Z_2 - Z_1}{Z_2 + Z_1} = \frac{\rho_2 v_2 - Z_1}{\rho_2 v_2 + Z_1} = A + \frac{B'}{c\phi + d'}, \quad (6c)$$

where $A = \frac{a}{c}$ and $B' = b' - \frac{a}{c} d'$.

$$\begin{aligned} a &= (\rho_w - \rho_{ma}) - Z_1 (\Delta t_w - \Delta t_{ma}); & b' &= \rho_{ma} - Z_1 \Delta t_{ma} + (\rho_{sh} - \rho_{ma} - Z_1 \Delta t_{sh} + Z_1 \Delta t_{ma}) V_{sh}; \\ c &= (\rho_w - \rho_{ma}) + Z_1 (\Delta t_w - \Delta t_{ma}); & d' &= \rho_{ma} + Z_1 \Delta t_{ma} + (\rho_{sh} - \rho_{ma} + Z_1 \Delta t_{sh} - Z_1 \Delta t_{ma}) V_{sh}. \end{aligned}$$

Workflow of porosity spectrum calculation and porosity segmentation

The whole workflow of porosity spectrum calculation and porosity segmentation is shown in Fig. 4.

Calculation workflow of porosity spectrum

Using ultrasonic imaging data to build porosity spectrum can be divided into five steps:

Step 1: Based on Eq. (4b) or (5), use the mud wave impedance Z_1 and conventional density and acoustic

wireline logs (e.g. DEN and AC) data to calculate formation reflection coefficient β' .

$$\beta' = \frac{Z_2 - Z_1}{Z_2 + Z_1} = \frac{\frac{\rho_2}{\Delta t_2} - Z_1}{\frac{\rho_2}{\Delta t_2} + Z_1}. \quad (7a)$$

Step 2: Introduce the echo response Eq. (1) and input transmitting amplitude A_0 , received echo amplitude AMP_i and echo traveling time TIM_i at the i th point in the depth of total n points to calculate attenuation factor τ , and

$$\overline{\text{LnAMP}} = \sum_{i=0}^n \ln(AMP_i), \quad \overline{\text{TIM}} = \sum_{i=0}^n TIM_i \quad \text{and} \\ \bar{L} = \overline{\text{TIM}} \times v_0.$$

Then, Eq. (1) can be turned into:

$$\frac{\overline{\text{LnAMP}}}{\text{Ln}A_0} = \text{Ln}\beta' - \alpha \times v_0 \times \overline{\text{TIM}}, \quad (7b)$$

where \bar{L} is the average distance from the transducer to the wall at the same depth; v_0 is the ultrasonic velocity in the mud.

Step 3: The τ can be set to be attenuation factor:

$$\tau = \alpha \times v_0. \quad (7c)$$

The attenuation factor τ at the depth can be obtained:

$$\tau = \frac{\text{Ln}\beta' - \frac{\overline{\text{LnAMP}}}{\text{Ln}A_0}}{\overline{\text{TIM}}}. \quad (7d)$$

Step 4: Substitute τ into Eq. (1), and use AMP_i and TIM_i to calculate reflection coefficient β_i of the pixel.

$$\beta_i = \frac{AMP_i}{A_0 \times e^{-\tau \times TIM_i}}. \quad (7e)$$

Step 5: Substitute β_i to Eqs. (4d), (5) or (6c), and then we can calculate the porosity value of each pixel which should be added up in equal depth spacing to draw porosity spectrum.

In addition, due to the porosity spectra transformation from ultrasonic images is based on rock volume model, the

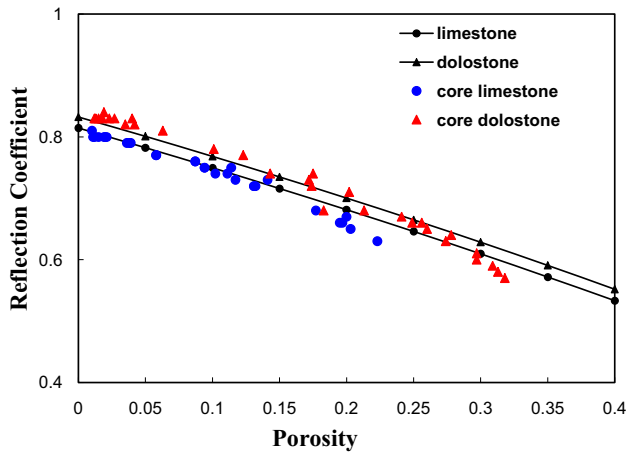


Fig. 2 The relationship between reflection coefficient and porosity in both pure calcite and dolomite matrix models deduced using Wyllie equation. The blue dots and red triangles are from experimental data, and the black curves with dots and triangles are from the conversion of Wyllie equation. Drilling mud wave impedance is $1850 \text{ g/cm}^3 \text{ m/s}$

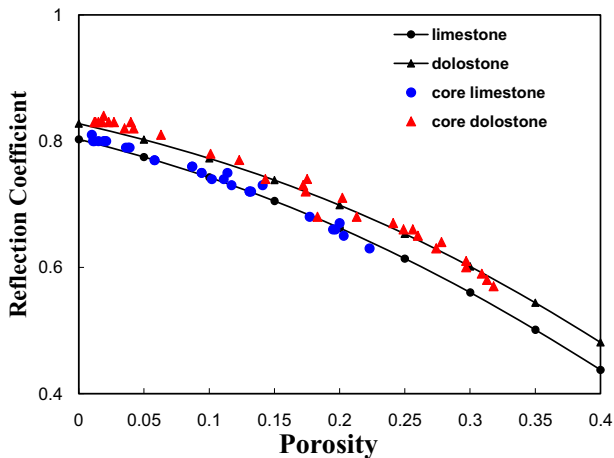


Fig. 3 The relationship between reflection coefficient and porosity in both pure calcite and dolomite matrix models deduced using Raymer equation. The blue dots and red triangles are from experimental data, and the black curves with dots and triangles are from the conversion of Raymer equation ($m = 2.5$). Drilling mud wave impedance is $1850 \text{ g/cm}^3 \text{ m/s}$

porosity spectrum transformation model is only applicable under the conditions that the lithology is simple, and porosity distribution is near-homogeneous and porosity variety is small.

The segmentation of primary and secondary porosity

Porosity spectrum usually presents two or three separate peaks. Small apertures correspond with high cumulative frequency, large range of variation, while the large ones

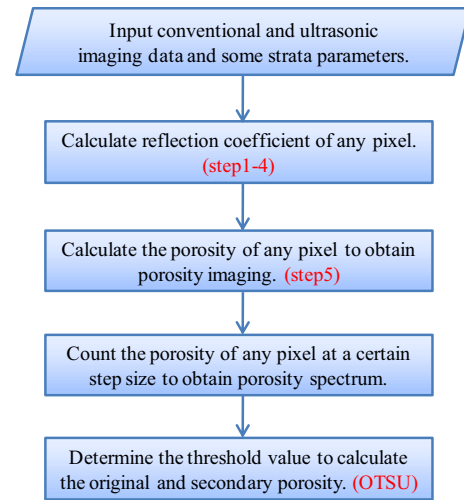


Fig. 4 The calculation workflow chart of obtain primary and secondary porosity from ultrasonic images

correspond with low cumulative frequency, small range of variation (Wang 2011). This phenomenon exactly reflects the state of primary pore and secondary pore in the underground rock. Thus, the frequency diagram can be used to distinguish original and secondary pore to obtain the two porosities, respectively. The methods to determine the threshold value between primary and secondary porosities mainly include artificial threshold division method (Wang 2011) and OTSU method (Otsu 1979).

OTSU method is an algorithm determining the image binarization threshold segmentation, which can execute image binarization segmentation to make the interclass variance between foreground and background image maximum.

Assuming the size of porosity image I is $M \times N$ pixels; secondary porosity (foreground) and primary porosity (background) segmentation threshold is t ; the ratio of number of pixels in the foreground to the whole image is m_0 ; average porosity is ϕ_0 ; the ratio of number of pixels in the background and the whole image is m_1 ; average porosity is ϕ_1 . The total average porosity of porosity image is ϕ_a ; Variance between classes is g . Consequently, the next equation can be obtained:

$$g = m_0 m_1 (\phi_0 - \phi_1)^2. \tag{8}$$

Ergodic methods should be taken to make the interclass variance g largest to obtain the threshold t between the original and secondary porosity, average original porosity ϕ_0 and average secondary porosity ϕ_1 .

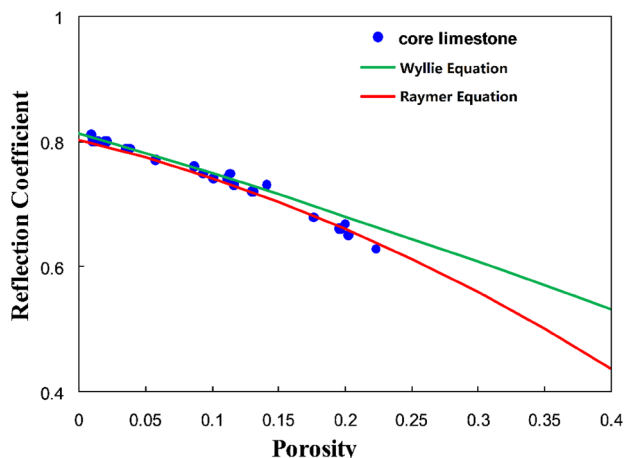


Fig. 5 Comparison diagram of the relationship between reflection coefficient and porosity deduced using Wyllie and Raymer equations in pure calcite matrix model. Blue dots are from experimental data (Chelini et al. 1998). Green and red curves are, respectively, obtained by Wyllie and Raymer equations ($m = 2.5$). Drilling mud wave impedance is $1850 \text{ g/cm}^3 \text{ m/s}$

Comparison studies and applicable condition analysis

In this section, different application effects of the above three conversion models (i.e. Wyllie and Raymer equations, and argillaceous matrix model) are studied, and by processing real data, the effect of converted ultrasonic images to porosity images and spectra are verified by comparison to micro-resistivity imaging logging.

Comparison of conversion models

As Fig. 5 shows, when reflection coefficient is small, the gap between the porosity converted by Wyllie and Raymer equations is big. It indicates that when the porosity is less than 15%, the Wyllie and Raymer equations are both suitable for the calculation in limestone formation with pure calcite matrix, but when the porosity is more than 15%, the porosity calculated by Wyllie equations is larger than Raymer equations. It reveals that the Raymer equation has a wider range of application in porosity calculation. Figure 6 shows an actual case of the difference between the two models. In this interval, there are two vertical fractures. The color of cracks in the first porosity image is darker than that in the second, and that means the porosity values of the fractures calculated from Wyllie equation are

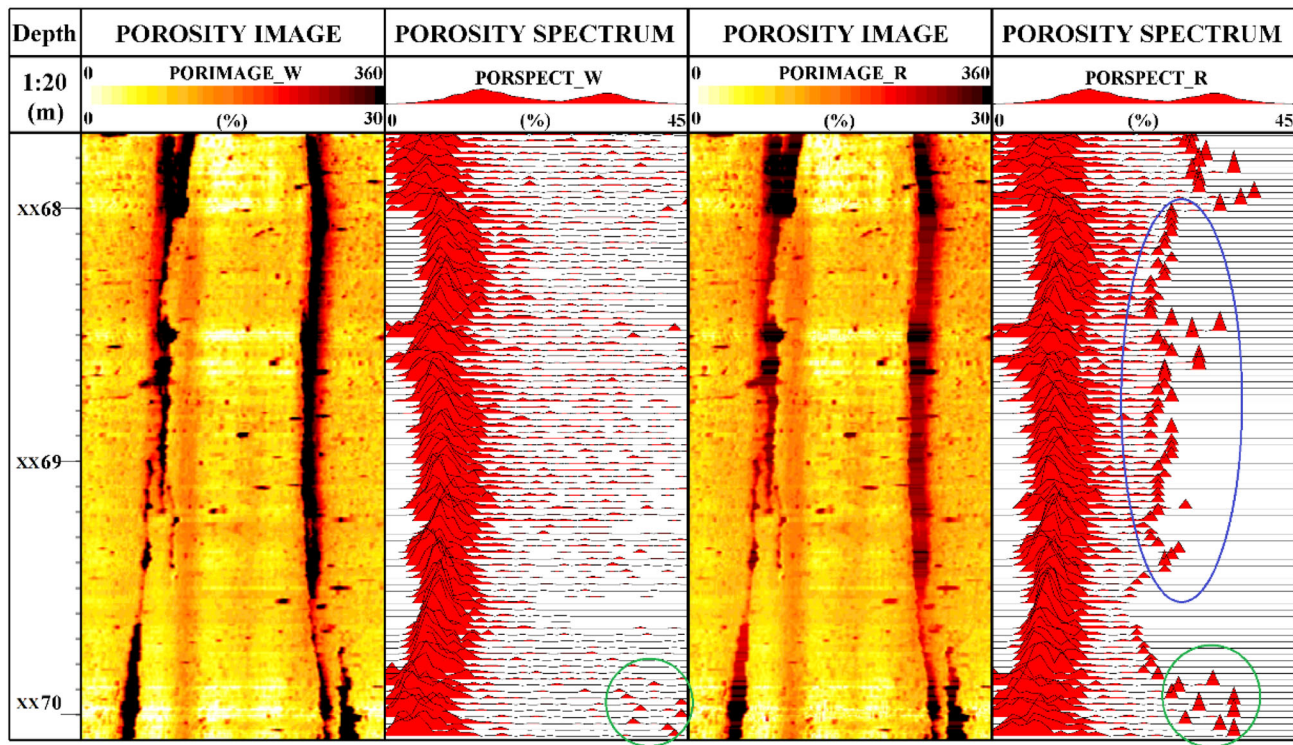


Fig. 6 The porosity images and spectra converted using Wyllie and Raymer models. From left: depth, porosity image computed using Wyllie equation, the spectrum of the Wyllie porosity image, porosity

image computed using Raymer equation, and the spectrum of the Raymer porosity image

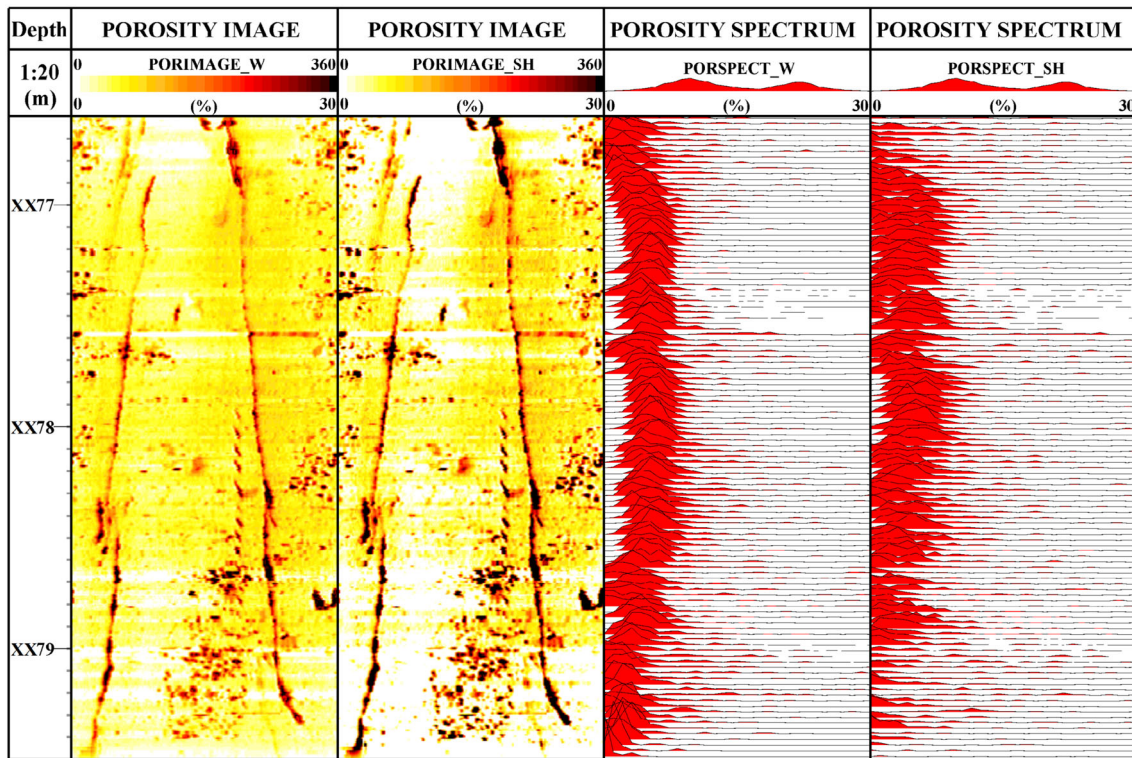


Fig. 7 The porosity images and spectra converted based on bulk-volume rock models without and with shale correction. From left: depth, porosity image without correction, porosity image with

correction, the spectrum of the porosity image without correction, and the spectrum of the porosity image with correction

higher. This results in the porosity value of the peaks appearing in the right (circled by green ellipses) in the Raymer result are smaller than the ones in the Wyllie result. And because the higher fracture porosities in Wyllie result are more concentrated, the count is low. Thus, the peaks in the Raymer results (circled by blue ellipse) are not so obvious in the Wyllie result.

Comparison of pre- and post-shale correction

In addition, the models converted by Wyllie and Raymer equations are only suitable in the formations with pure calcite and dolomite matrix, but not with too much shale. Figure 7 shows the conversion results of models of bulk-volume rock with or without shale correction. In the porosity images, the shade of color represents the magnitude of porosity. After shale correction, the color of porosity image is lighter, and the spectra move left along with lower peaks. The shale content (V_{sh}) is calculated by natural gamma ray logs (GR) using follow equations (Larionov 1969):

$$SH = (GR - GR_{min}) / (GR_{max} - GR_{min}), \quad (9a)$$

$$V_{sh} = (2^{g_{cur} \times SH} - 1) / (2^{g_{cur}} - 1), \quad (9b)$$

where the SH is the original shale content, GR_{min} and GR_{max} are, respectively, the GR values of carbonate stone and pure mudstone formation. The g_{cur} is the correction coefficient, which is 2 in older strata and 3.7 in newer strata.

Comparison of ultrasonic and micro-resistivity imaging logging

Thanks to the works of predecessors, the technology of converting micro-resistivity images to porosity images is proved to be mature and valid (Tyagi and Bhaduri 2002). In this section, we compare the conversion results of ultrasonic and micro-resistivity images. In Fig. 8, the secondary pores are very clear in ultrasonic porosity image, but not in the resistivity one. Anyway, the trends of them and the modes reflecting formation information are similar except the distribution range of ultrasonic spectrum is wider. It is conspicuous that the secondary porosities calculated by ultrasonic and resistivity spectra are near except the part circled by green ellipse. In this part, the secondary porosity of ultrasonic image is significantly larger than resistivity image because of the dissolved pores measured by ultrasonic imaging logging are more obvious (black dots in the image). Therefore, the method of converting

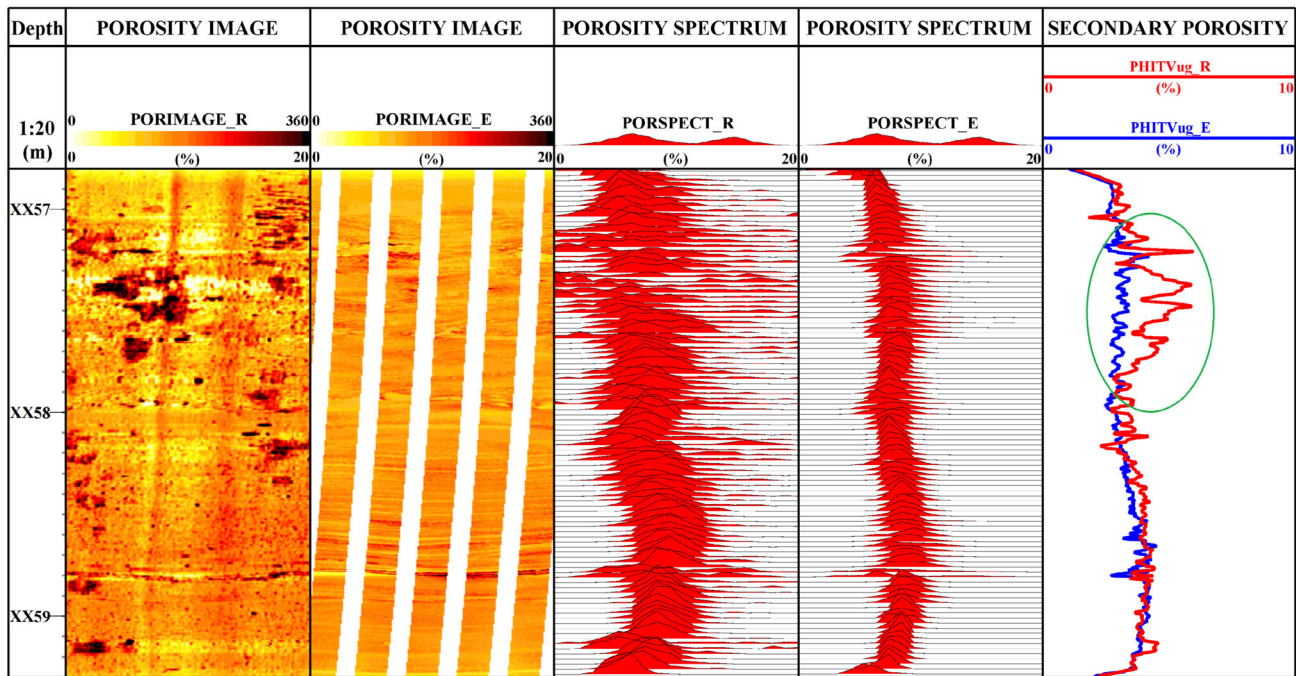


Fig. 8 The ultrasonic and micro-resistivity imaging porosity images and spectrum analysis. From left: depth, ultrasonic borehole wall porosity image, unfilled micro-resistivity borehole porosity image, the spectrum of ultrasonic porosity image, the spectrum of micro-

resistivity porosity image, the secondary porosity curves calculated from the two images (red for ultrasonic and blue for micro-resistivity, the porosity range is 0–10%)

ultrasonic images to porosity images and spectra, even to calculate the primary and secondary porosity is workable.

spectrum, etc. Therefore, the quality of imaging logging is very important for applying this conversion method.

Analysis of applicable conditions

The measurement of ultrasonic imaging logging tools is based on the transducer that is located in the center of a round borehole of which the caliper is regular. Due to the influence of the borehole shape and tool eccentricity, acoustic signal propagation time in the drilling mud will vary with location. Even if the well wall medium is uniform, it can also result in a heterogeneous imaging logging image. When some or the entire reflected acoustic wave cannot be received by the transducer, the echo amplitude will decline seriously, so that the imaging logging image will present vertical black stripes significantly.

Porosity obtained via ultrasonic imaging logs introduce echo amplitude and the echo time as important inputs, therefore its transformation effect will be affected by the borehole shape and tool eccentricity significantly. When the tool is in an elliptical borehole, ultrasonic logging image will appear as two dark black stripes, which will affect the identification of cracks; when the tool is not in the hole center, black vertical stripes will appear on imaging logging image, and they also appear on porosity image, which will hide the details on borehole wall, so porosity spectrum can show up abnormal, such as loss of

Case study

In this study, our data for application are from a well LXX in the Tianhuan Depression, Ordos Basin in Northwestern China. The application result is shown in Fig. 9.

Figure 9 is the porosity spectrum analysis results image, generated from the ultrasonic imaging log from the interval of XX43–XX63m in LXX well using the workflow presented in this paper. Porosity images in track 6 and track 7 can reflect the size of the porosity from the shade in the image. They can not only help us distinguish pore type of the reservoir, but also reveal the size change of the primary porosity intuitively and clearly. Track 8 is ultrasonic imaging spectrum transformed from pure calcite matrix porosity model. The forms of porosity spectrum curve are unimodal, bimodal or multi-peak, associated with the reservoir heterogeneity. Compared to resistivity porosity spectrum in track 9, the shape of ultrasonic porosity spectrum track 8 is similar, but its spectral peak is wider relatively. This may be caused by the lower sensitivity of the porosity to the wave attenuation.

The secondary porosity in depth XX47–XX48m is poor developed, so the porosity spectrum is narrower and

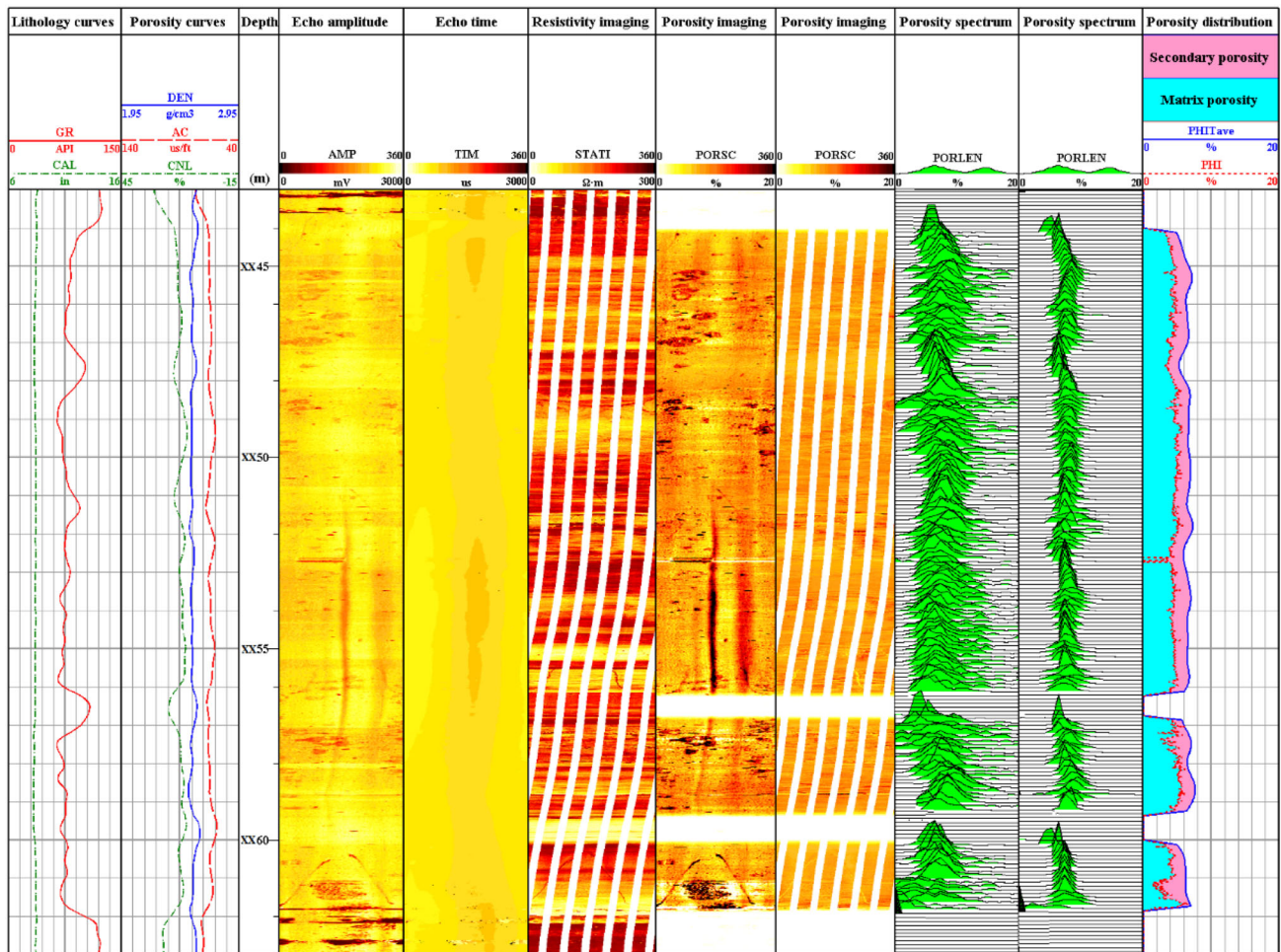


Fig. 9 Well LXX (XX43m–XX63m) porosity spectrum analysis results. Track 1: GR 0–150 API, CAL 6–16 in.; track 2: DEN 1.95–2.95 g/cm^3 , AC 140–40 $\mu\text{s}/\text{ft}$, CNL 45–15%; track 3 and track 4 are ultrasonic echo amplitude and echo time image; track 5 is static resistivity imaging; track 6 and track 7 are ultrasonic imaging and

resistivity porosity image, 0–20%; track 8 and track 9 are ultrasonic imaging and resistivity porosity image, 0–20%; track 10 is porosity distribution, PHI and PHITave represent the primary porosity and total average porosity, respectively, 0–20%

unimodal; In depth intervals XX45–XX47m, XX57–XX57.8m and XX61–XX61.6m, different scales of secondary pores resulted from dissolution are visible, therefore, the porosity spectrum shows wider bimodal or multimodal spectra with lower peaks; In depth interval XX60.3–XX61.6m high conductivity fractures caused by drilling mud invasion or argillaceous filling develop, and their porosity presents wider unimodal or bimodal spectra. In depth interval XX53.7–XX56.2m, there is not any vertical fracture in the resistivity image, but two dark vertical stripes are found in the ultrasonic image. That means the ultrasonic tool eccentric position may occur at this depth section. The stripes are mistaken for vertical fractures in analysis workflow, and that causes the ultrasonic porosity spectrum wider than resistivity porosity spectrum. This reveals that the measurement quality of ultrasonic imaging affect the effect of porosity spectrum directly.

Track 10 in Fig. 9 is primary and secondary porosity calculated by porosity image quantitatively based on OTSU method. It is obvious that the matrix porosity of the reservoir section is very stable, about 5–6%; Secondary porosity is about 2%, increasing obviously in intervals where different scale dissolved pores develop.

In general, the results show that the method is applicable and the application result depends on the logging quality.

Conclusions

In this paper, we provide a new way to evaluate the dual-porosity systems in carbonate formation using ultrasonic borehole images. This is a new integrated workflow to establish the relationship between the reflected wave amplitude and reflection coefficient which carry

information about formation porosity. Based on models of bulk-volume rock and Raymer equation, three porosity conversion models suitable for pure and shaly matrix have been provided and verified. From the whole research, we can come to several conclusions as follows:

1. Based on bulk-volume rock models, we establish the conversion relationship between reflection coefficient of drilling mud and formation interface and the formation porosity, discovering that the reflection coefficient decreases in an inverse proportion function as the porosity increases.
2. Based on reflected wave amplitude attenuation equation and the bulk-volume rock models, we can use conventional well logging curves such as the formation density and acoustic interval transit time and ultrasonic imaging data such as echo amplitude and traveling time to get porosity distribution image and porosity spectrum.
3. OTSU method can be effectively used to determine the threshold of the primary and secondary porosity and precisely calculate the primary and secondary porosity of reservoir, which is meaningful to quantitative analysis of the fracture development degree of the reservoir.
4. The spectrum analysis method for ultrasonic imaging is similar to the one used in resistivity imaging. Under the same geological condition, the shapes of porosity spectra from ultrasonic and resistivity imaging logs are similar, but the spectrum peak range is relatively wider in results from ultrasonic imaging which may occur due to the lower sensitivity of the porosity to the wave attenuation.
5. Compared to micro-resistivity borehole images, ultrasonic borehole images can cover 100% of borehole wall, so it can provide more complete strata porosity information (e.g. vugs and fractures, etc.). However, because of the sensitivity of ultrasonic imaging tools, the imaging result can be affected by many factors such as the borehole shape condition or tool position. Therefore, the application condition of our workflow is very rigorous and we should consider the imaging quality first, and use the pore spectrum result with caution. It is better to use the spectra obtained from both ultrasonic and resistivity imaging logging data together to analyze the porosity.

Acknowledgements This research is supported by National Natural Science Foundation of China (Grant nos. 41504094 and 41404084). The authors thank the editor and the two reviewers for their constructional comments and suggestions. Dr. Xin Nie's visiting research in Georgia Institute of Technology is supported by China Scholarship Council (CSC).

Compliance with ethical standards

Conflict of interest On behalf of all authors, the corresponding author states that there is no conflict of interest.

References

- Akbar M, Chakravorty S, Russell SD, et al (2000) Unconventional approach to resolving primary and secondary porosity in Gulf carbonates from conventional logs and borehole images. In: SPE paper 87297-MS presented at the Abu Dhabi international petroleum conference and exhibition
- Chelini V, Meazza O, and Verhoeff EK (1998) Relations between ultrasonic amplitude and petrophysical characteristics. In: SPE paper 50606-MS presented at the European petroleum conference
- Ghafoori MR, Roostaeian M, Sajjadian VA (2009) Secondary porosity: a key parameter controlling the hydrocarbon production in heterogeneous carbonate reservoirs (case study). *Petrophysics* 50(1):68–78
- Gu Y, Bao Z, Lin Y, Qin Z, Lu J, Wang H (2017) The porosity and permeability prediction methods for carbonate reservoirs with extremely limited logging data: stepwise regression vs. N-way analysis of variance. *J Nat Gas Sci Eng* 42:99–119. <https://doi.org/10.1016/j.jngse.2017.03.010>
- Hurley NF, Zimmermann RA, and Pantoja D (1998) Quantification of vuggy porosity in a dolomite reservoir from borehole images and core, Dagger Draw field, New Mexico. In: SPE paper 49323-MS presented at the SPE international technical conference and exhibition
- Larionov VV (1969) Radiometry of boreholes. NEDRA, Moscow (**in Russian**)
- Newberry BM, Grace LM, and Stief DD (1996) Analysis of carbonate dual porosity system from borehole electrical images. In: SPE paper 35158-MS presented at the Permian basin oil and gas recovery conference
- Otsu N (1979) A threshold selection method from gray-level histograms. *IEEE Trans Syst Man Cybern* 9:62–66. <https://doi.org/10.1109/TSMC.1979.4310076>
- Raymer LL, Hunt ER, and Gardner JS (1980) An improved sonic transit time-to-porosity transform. In: SPWLA 21st annual logging symposium, paper P
- Tetsushi Y, Daniel Q, Arnaud E et al (2013) Revisiting porosity analysis from electrical borehole images: integration of advanced texture and porosity analysis. In: SPWLA 54th annual logging symposium, paper E
- Tyagi AK and Bhaduri A (2002) Porosity analysis using borehole electrical images in carbonate reservoirs. In: SPWLA 43rd annual logging symposium, paper KK
- Urick RL (1948) The absorption of sound in suspensions of irregular particles. *J Acoust Soc Am* 20(3):283–289
- Urick RL, Ament WS (1949) The propagation of sound in composite media. *J Acoust Soc Am* 21(1):62
- Wang Z (2011) Application researching of the quantitative interpretation of borehole resistivity and acoustic imaging logging in fractured reservoir. Dissertation, China University of Petroleum, East China
- Wang H, Tao G (2011) Wavefield simulation and data-acquisition-scheme analysis for LWD acoustic tools in very slow formations. *Geophysics* 76(3):E59–E68
- Wang H, Fehler MC, Miller D (2017) Reliability of velocity measurements made by monopole acoustic logging-while-drilling tools in fast formations. *Geophysics* 82(4):D225–D233. <https://doi.org/10.1190/geo2016-0387.1>

- Wyllie MRJ, Gregory AR, Gardner LW (1956) Elastic wave velocities in heterogeneous and porous media. *Geophysics* 21(1):41–70
- Wyllie MRJ, Gregory AR, Gardner LW (1958) An experimental investigation of factors affecting elastic wave velocities in porous media. *Geophysics* 23(3):459–493
- Xu C, Richter P, Russell D, Gournay J (2006) Porosity partitioning and permeability quantification in vuggy carbonates using wireline logs, Permian basin, west Texas. *Petrophysics* 47(1):13–22